Research Article

Angewandte International Edition Chemie
www.angewandte.org

How to cite: *Angew. Chem. Int. Ed.* **2025**, e202503618
doi.org/10.1002/anie.202503618

Porous Coordination Polymers

Pore Engineering in Isoreticular Titanium-Isophthalate Coordination Polymers

Qingqing Yan+, Chenyang Nie+, Valentin Diez Cabanes+, Fu-An Guo+, Yafei Du, Hailun Xia, Hao Wang, Guillaume Maurin,* Peng Guo,* and Sujing Wang**

Abstract: Pore engineering through chemical environment modification is vital for developing industrial porous materials. Understanding the effects of substitutions in isoreticular porous coordination polymers—such as steric hindrance, vibrational capabilities, electronic influences, and hydropathy—is key to elucidating structure–property relationships. However, accurately assessing the impact of functional groups on properties remains challenging due to limitations in current methodologies. In this study, we designed a series of titanium-isophthalate coordination-polymers with various functional groups to regulate pore characteristics and structural dimensionality. The unique spatial arrangement and electronic distribution of isophthalate and its functional groups provide an ideal platform to address these challenges. We conducted extensive investigations combining experimental methods with computational simulations to explore how pore engineering affects adsorptive separation and photoresponsive behavior in these compounds. Our findings not only tackle the synthesis challenge of isostructural titanium-coordination polymers but also offer new insights into understanding structure–property relationships achieved through modulation of their chemical environments.

Introduction

Pore engineering, in terms of shape, size, and chemical environment, is essential for the advancement of porous materials, particularly those utilized in industrially significant processes, such as chemical separation, substance storage, and heterogeneous catalysis.[1,2] Among the various types of porous materials known, porous coordination polymers (PCPs) are renowned for their limitless combinations of inorganic structural units and organic linkers, offering great potential for porosity engineering.[3,4] Specifically, the principle of reticular chemistry enables rational and systematic exploration of functionalized and modified metal–organic frameworks (MOFs).[5,6] This underscores the critical importance of comprehending the structure–property relationship in experimental studies, which is essential for further advancements in this research field.

In general, the reticular expansion of a certain MOF structure can be achieved by modifying linker characteristics, such as molecular length (the distance between coordination sites), width (size of the moiety along the molecular direction without coordination sites), and substituted functional groups.[7,8] The feasibility of reticular expansion largely depends on how sensitive and compatible the metal nodes are to changes in linker characteristics under similar reaction conditions. Increasing the molecular length of linkers has contributed significantly to achieving a series of reticular structures with adjustable pore sizes. This is evident from numerous reported examples, as adding extra conjugated chemical bonds to pristine linker moieties primarily affects solubility but has a limited influence on the coordinative environments for building networks.[9,10] As a result, changes in pore size—unlike alterations in the chemical environment—in these reticular materials offer limited insights into the investigation of structure–property relationships.

In contrast, the substitution of functional groups on the linker can lead to direct engineering of the chemical environment within the pore. This results in a diverse range of outcomes, thereby providing an ideal platform for understanding the structure–property relationships in isostructural

---

[*] Q. Yan+, Y. Du, S. Wang
Laboratory of Spin Magnetic Resonance, Suzhou Institute for Advanced Research, Hefei National Laboratory, University of Science and Technology of China, Hefei 230026, China
E-mail: sjwang4@ustc.edu.cn

C. Nie+, P. Guo
National Engineering Research Center of Lower-Carbon Catalysis Technology, Dalian Institute of Chemical Physics, Chinese Academy of Sciences, Dalian 116023, China
E-mail: pguo@dicp.ac.cn

C. Nie+, P. Guo
University of Chinese Academy of Science, Beijing 100049, China

V. D. Cabanes+, G. Maurin
ICGM, University of Montpellier, CNRS, ENSCM, Montpellier, France
E-mail: guillaume.maurin1@umontpellier.fr

F.-A. Guo+, H. Xia, H. Wang
Hoffmann Institute of Advanced Materials, Shenzhen Polytechnic University, Shenzhen 518055, China
E-mail: wanghao@szpu.edu.cn

G. Maurin
Institut Universitaire de France (IUF), Paris, France

[+] These authors contributed equally to this work.

Additional supporting information can be found online in the Supporting Information section series of materials. The impact of substitution is contingent upon the distance between the substituted and coordinative sites, as well as the level of conjugation of the moiety involved. In the case of large linker molecules, substitution at a sufficient distance from the coordination site does not significantly affect isoreticular synthesis, demonstrating good tolerance to different MOFs.[11,12] However, complex organic synthesis has greatly restricted the diversity of functional groups involved. Conversely, for commercially available simple linkers, such as terephthalic acid and imidazole, functional group substitution can lead to significant steric hindrance and an electron density shift in the coordinative site, resulting in noticeable differences in the synthesis of isoreticular materials. Consequently, there are limited examples of systematic isoreticular structure expansion found in the literature, including IRMOFs[8] (IRMOFs: Isoreticular MOFs), MIL-53[13] (MIL: Materials from Institut Lavoisier), MIL-101,[14] UiO-66[15] (UiO: University of Oslo), and imidazole-based ZIFs[16] (ZIFs: Zeolitic Imidazolate Frameworks), among others.

Accurately discerning the individual effects of each parameter associated with various substitutions on the corresponding properties of isostructural materials is highly challenging. The resultant property emerges as a synergistic outcome of multiple parameters linked to each substitution, including steric hindrance, stretching and vibrational capabilities, electronic influences, and hydropathy characteristics. This complexity considerably complicates our understanding of the structure–property relationship. Consequently, advancements in material research and the development of reticular chemistry are imperative for discovering new series of isoreticular MOFs based on simple linkers—particularly cost-effective industrial feedstocks. Such developments will enable precise differentiation of the effects related to specific substitutions; an achievement that remains elusive yet critically important for increasing our comprehension of structure–property relationships.

In this study, we present isoreticular titanium coordination frameworks synthesized directly using a cyclic 8-connected Ti_8O_8 inorganic building unit in conjunction with isophthalic acid and its derivatives. The structural dimensionality has been expanded from two-dimensional (2D) layers to three-dimensional (3D) frameworks, designated as USTC-701 and USTC-702, respectively (USTC: University of Science and Technology of China). We rigorously investigated the mechanisms underlying this dimensional expansion through advanced computational calculations and simulations. The diverse functional substituents incorporated into these structures provide significant flexibility in modulating pore size, shape, and chemical environment. This pore engineering adaptability facilitates a comprehensive assessment of the effects associated with specific substitutional groups, resulting in tunable performance for gas and vapor sorption as well as separations. Furthermore, we conducted an extensive investigation that combined experimental methods with computational simulations to explore the structure–property relationships concerning the impact of pore engineering on the photoresponsive behavior of these compounds. Our findings indicate that regulating pore characteristics through strategic incorporation of functional groups not only enhances physical application performance—such as adsorptive separation—but also aligns crystal structure with electronic properties for various chemical applications, including photocatalysis.

Results and Discussion

Titanium coordination polymers constitute an underdeveloped research field in coordinative materials, with fewer than 60 examples reported over the past decades.[17] This is mainly due to the challenge of controlling titanium chemistry in direct synthesis.[18] However, encouraging progress has been made in the isoreticular expansion and pore size tuning of several Ti-MOF families, such as MOF-901/902,[19] ZSTU-1/2/3[20] (ZSTU: Zhejiang Sci-Tech University), and UCFMOF-2/3/4[21] (UCF: University of Central Florida), through multistep organic synthesis of complex linkers via the linker length alteration strategy. This progress reflects the difficulty of forming corresponding isostructures when functional group substitution occurs on short and simple linkers. To date, only MIL-125[22] has been reported to have an amino-functionalized isostructure.[23] However, this isostructure exhibits significantly enhanced stability, photoresponsiveness, and catalytic activity,[24] underscoring the appeal of isoreticular structural expansion. This also prompts further exploration of other isoreticular series of titanium coordination polymers.

Notably, the cyclic Ti_8O_8 inorganic building unit in MIL-125 has a notable ability to adapt to diverse connection numbers and configurations when used to fabricate coordinative frameworks, which highly depends on the characteristics of the linker involved (Figure 1). Owing to charge balance, there are a maximum of sixteen carboxylate groups present on this octanuclear cluster, corresponding to the maximum possible connection number of 16, as observed in the FIR-125 and -126 structures (Figure 1a, FIR: Fujian Institute of Research on the Structure of Matter). The structural flexibility of the linkers for FIR-125 and -126 allows for an optimal spatial arrangement around the Ti_8O_8 cluster, resulting in the full connection number.[25] In contrast, the terephthalic acid (BDC) that forms the MIL-125 structure is rigid and creates significant repulsion between neighboring benzene rings in a crowded coordinative environment when the 16-connection mode is utilized. Therefore, the 12-connection mode is preferred to reduce the energy required for structure stabilization, and four hydroxyl groups are observed instead of carboxylates to further optimize space accommodation (Figure 1b). The coordination number of the Ti_8O_8 cluster could be further reduced to eight in the MIP-207[26] structure (MIP: Materials of the Institute of Porous Materials from Paris). In this structure, the trimesic linker utilizes two carboxylate groups at meta positions to connect neighboring inorganic units, resulting in increased steric hindrance compared with that of the linkers in MIL-125 and FIR-125 (see Figure 1c). Therefore, this cyclic Ti_8O_8 cluster demonstrates the highest level of connection flexibility among all the inorganic building units found in reported titanium coordination polymers. This may be comparable to or even more diverse than the various connection numbers observed

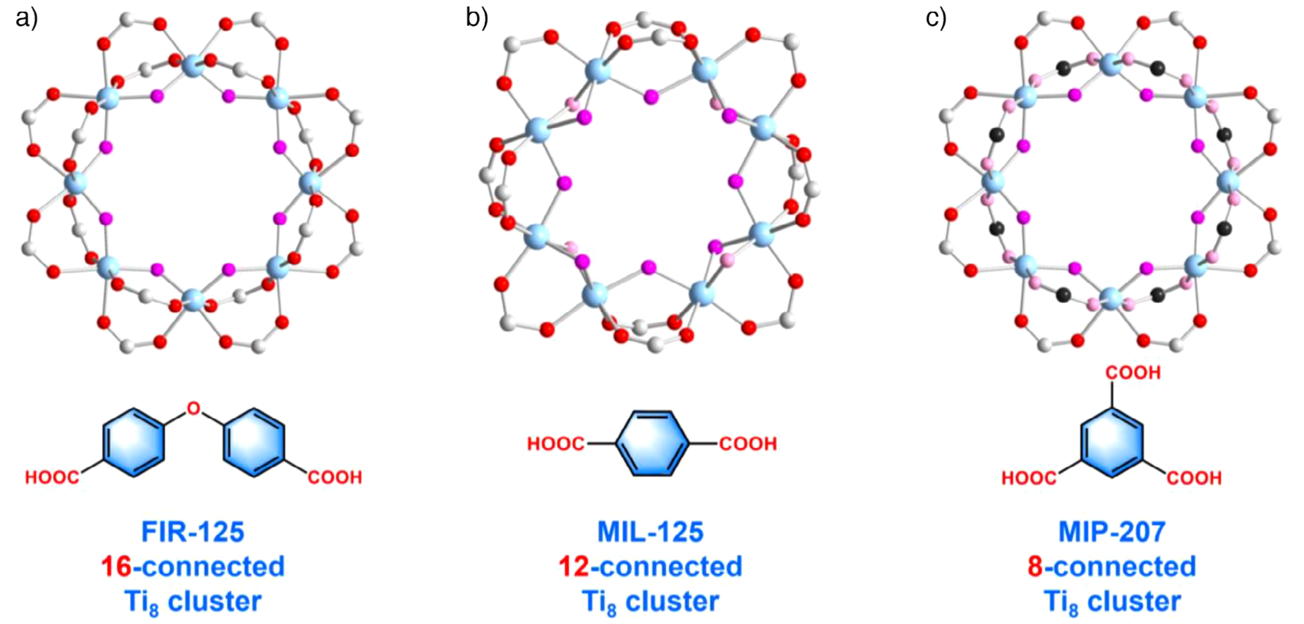

Figure 1. Comparison of reported cyclic Ti_8O_8 clusters. a) A 16-connected Ti_8O_8 cluster is observed in the crystal structure of FIR-125 as the inorganic building unit, demonstrating a fully connected mode resulting from the structural flexibility of the linker. b) The crystal structure of MIL-125 reveals a 12-connected Ti_8O_8 cluster building unit, showing a decreased connection number compared with that in the fully connected mode due to the steric hindrance of the terephthalate linker in the spatial arrangement. c) In the crystal structure of MIP-207, an 8-connected Ti_8O_8 cluster building unit is observed, indicating a further decrease in the number of connections as a result of increased steric hindrance of the trimesic linker in the spatial arrangement. Ti, blue; C in the linker carboxylate group, light gray; C in the terminal ligand, dark gray; O in the linker carboxylate group, red; O in the terminal ligand and bridging hydroxyl group, light red; O in the bridging oxo group, pink.

in Zr_6 cluster-based coordination polymers.[27] Specifically, the 8-connection mode can accommodate functional group-substituted linker series, allowing for the theoretical potential to facilitate isostructural expansion.

Organic linkers with oxygen binding sites are most suitable for constructing titanium coordination polymers according to the hard–soft-acid–base theory proposed by Ralph G. Pearson.[28] In particular, isophthalic acid (IPA) is an ideal option for discovering a new series of isostructural coordination polymers on the basis of the following considerations: 1) The *meta*-arrangement of the two carboxylate groups on the benzene ring offers unique distances, angles, and cooperative possibilities. This leads to a significantly wider range of connection patterns than linear linkers such as terephthalic acid and fumaric acid. As a result, diverse MOF structures with ultramicroporosity,[29] microporosity,[30] and even mesoporosity[31] have been constructed from IPA-type linkers. 2) Common organic substitutions can be categorized into two distinct groups: ortho-para orienting and meta orienting. The former group includes alkyl, hydroxyl (-OH), amino (-NH_2), and halide groups, whereas the latter encompasses nitro (-NO_2), cyano (-CN), formyl (-CHO), trifluoromethyl (-CF_3), and carboxylate groups. These substitutions have the potential to induce various electronic effects on the positions of the benzene ring and may lead to steric hindrance at the coordination-active sites of linkers. Specifically, BDC-type linkers are limited in their ability to introduce functional groups at the ortho-position of the carboxylate on the benzene ring, resulting in steric hindrance and electronic density shift effects on at least one of the two carboxylate groups. This holds true regardless of whether the substitution is ortho-para orienting or meta orienting (such as 2-aminoterephthalic acid or 2-NH_2-BDC).

In contrast, IPA-type linkers present a completely different scenario. The functional groups are predominantly introduced at the fifth position on the benzene ring, providing sufficient separation from the coordination sites and thus causing almost no steric hindrance to the carboxylate groups at the two meta-positions. Consequently, a systematic study can be conducted to assess the major influences of the size and shape of functional groups on material pores by introducing ortho–para-orienting substitutions to this specific position on the benzene ring. These substituted groups have negligible electronic effects on meta-positional carboxylates (such as 5-aminoisophthalic acid and 5-NH_2-IPA). Moreover, with the introduction of meta-orienting groups at the fifth position of the benzene ring, functional groups not only exhibit size and shape effects but also undergo additional electronic modifications in relation to meta-positional carboxylates (such as 5-nitroisophthalic acid and 5-NO_2-IPA). As a result, the remarkable flexibility in linker selection for IPA-type compounds enables target-driven isoreticular chemistry, a feature that cannot be achieved with BDC-type linkers. Consequently, commercially available substituted IPA linkers with cost-effective features offer a wide range of functional groups at the fifth position of the benzene ring and serve as an ideal platform for investigating substitution effects on the pore characteristics of isostructural MOFs.

With the Ti_8 cluster and IPAs serving as fundamental building components, our initial approach involved

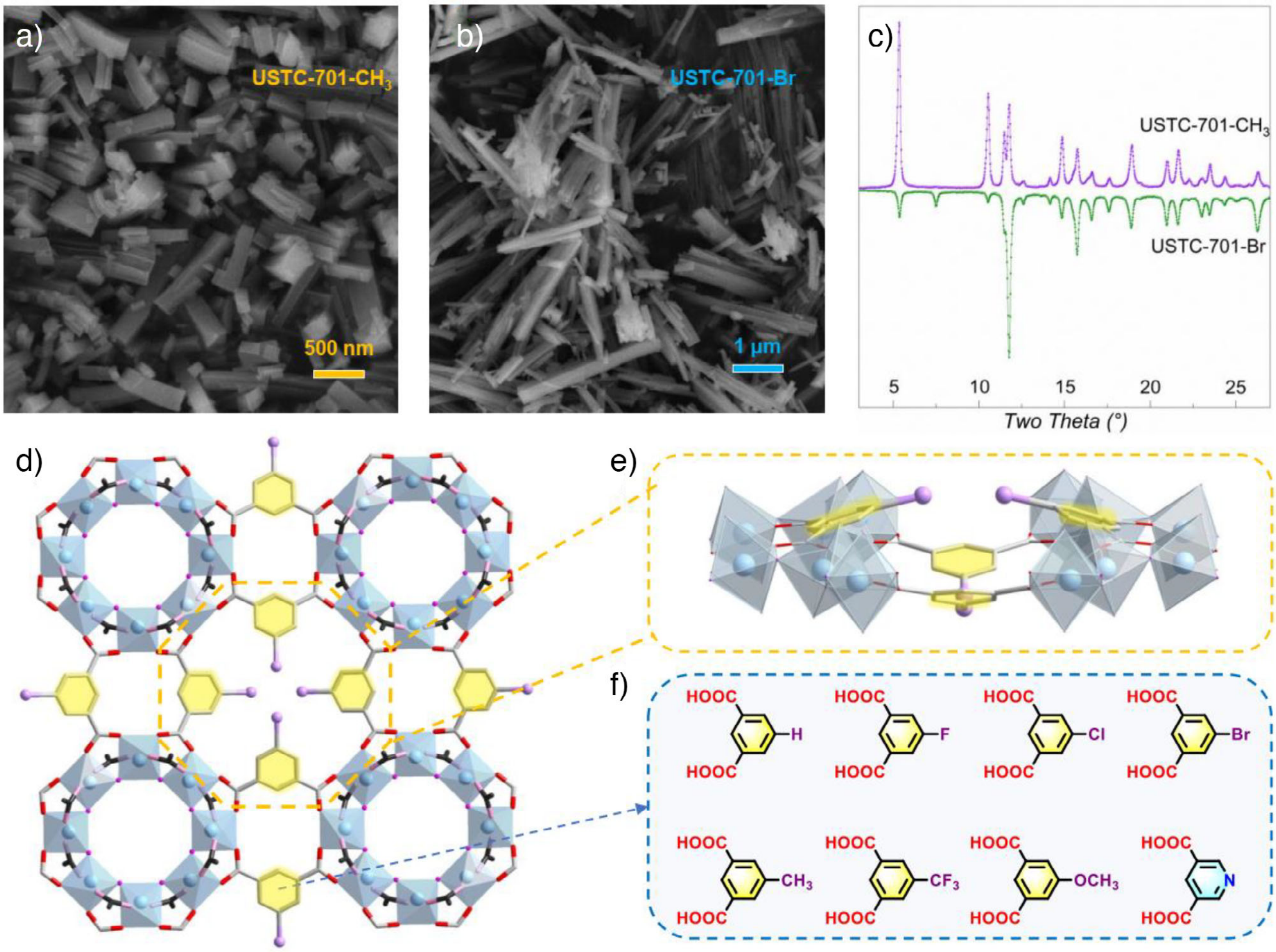

Figure 2. Structural information of USTC-701. a) SEM image of the USTC-701-CH$_3$ compound reveals a particle shape with a rectangular prism morphology. b) SEM image of the USTC-701-Br compound showing a rectangular needle morphology. c) Comparison of the PXRD patterns of USTC-701-CH$_3$ and USTC-701-Br, indicating different preferred crystal orientations. d) The 2D layered crystal structure of USTC-701, viewed along the *c*-axis, illustrates the connection between the Ti$_8$ cluster building unit and the IPA-type linker. e) Pore configuration, viewed slightly in the *ab* crystal plane direction, demonstrating the up and down mode of two pairs of IPA linkers that build the pore entrance. f) The scope of the substituted functional groups involved in this USTC-701 isostructural series. The color code is the same as that in Figure 1; functional groups substituted at the fifth position of the benzene ring of IPA-type linkers are represented in purple.

conducting synthesis attempts through the adoption of a linker-exchange strategy. This approach has been demonstrated to be effective in the synthesis of the MIP-207 compound when the Ti$_8$-acetate-formate (Ti$_8$AF) cluster precursor is employed.[26] 5-CH$_3$-IPA and the Ti$_8$AF cluster precursor were utilized to determine the optimal conditions for synthesizing the USTC-701 series after a systematic investigation of the reaction parameters (Methods and Note S1). Compared with the standard synthetic conditions of MIP-207, the reactions used to produce USTC-701 products exhibit good tolerance toward different functional groups (Figure S1), higher reaction temperatures (above 180 °C), and the addition of a small amount of methanol to increase product crystallinity. Notably, variations in functional groups lead to two distinct product morphologies: a rectangular prism shape represented by the USTC-701-CH$_3$ product (Figure 2a) and a rectangular long needle shape represented by the USTC-701-Br product (Figure 2b). The observed variations correspond to distinct preferred crystal orientations and relative intensity modifications in the powder X-ray diffraction (PXRD) patterns. Notably, however, good alignment of the peak positions for the -CH$_3$- and -Br-functionalized USTC-701 products can be discerned (Figure 2c and Figure S2).

To precisely confirm their isostructural characteristics, both the USTC-701-CH$_3$ and USTC-701-Br samples were subjected to advanced structure determination. Although conventional single-crystal X-ray diffraction (SCXRD) requires large crystals, the sub-micrometer dimensions of USTC-701 crystals preclude its application. The emerging continuous rotation electron diffraction (cRED), a state-of-the-art 3D electron diffraction technique, has proven particularly effective for solving structures of novel nanomaterials with unknown crystallography[1,32–37] (Figures S3 and S4, Tables S1–S4, and Note S2). Structural analysis revealed that both compounds crystallize in the tetragonal *P*4/*nbm* (125) space group with very similar unit-cell parameters.

Specifically, $a = b = 24.1$ Å and $c = 8.0$ Å for the -CH_3-substituted compound, and $a = b = 23.8$ Å and $c = 7.9$ Å for the -Br-substituted compound. These parameters correspond to the shared formula $Ti_8(oxo)_8(acetate)_8(IPAs)_4$[38]. As shown in Figure 2d, the Ti_8 cluster configuration remained unchanged in the USTC-701 structure after the terminal formates in the original Ti_8AF cluster were exchanged with IPA-type linkers. The eight bridging acetates remain undisturbed, whereas each Ti_8 cluster offers eight carboxylate linkage sites for attaching four pairs of IPAs, thereby connecting adjacent clusters. Consequently, the Ti_8 building unit can be simplified as a 4-connected node (Figure S5). Each linker molecule serves to bridge two neighboring Ti_8 clusters via its meta-positional carboxylates, with the separated functional group at the fifth position on the benzene ring oriented toward the structural pore, resulting in a 2D layered structure. The interactions between acetates in neighboring layers, along with van der Waals forces, contribute to a close-packed arrangement (Figure S6).

Importantly, the four functionalized linker molecules defining the pore shape, size, and chemical environment adopt an updown spatial arrangement to minimize steric hindrance. This gives rise to an irregular cavity passageway with potential local flexibility due to the rotational freedom of substitution (Figure 2e). The selection of functional substituents on the linker molecule is designed to be representative of both ortho-para orienting substitutions and meta-orienting substitutions. In addition to the nonfunctionalized IPA compound, modified linkers containing ortho-para orienting groups such as -F, -Cl, and -Br (strong to weak electron withdrawing) and -CH_3 (weak electron donating), as well as meta-orienting groups such as -CF_3 and -OCH_3 (medium to weak electron withdrawing), have been proven effective in synthesizing the USTC-701 isostructure. In addition, the heteroaromatic IPA-type compound 3,5-pyridine-dicarboxylic acid notably extends the linker scope. However, meta-orienting substitutions with a strong electron-withdrawing effect can significantly disrupt the formation of the expected isostructural product. For example, 5-NO_2-IPA resulted in complex products with much poorer crystallinity under similar reaction conditions. (Figure 2f and Figure S7).

To further assess the adaptability of the reaction conditions for IPA-type linkers, our focus shifted to dicarboxylic acids containing meta-positionally substituted five-membered heteroaromatic rings, such as 2,5-thiophene-dicarboxylic acid (TDA), 2,5-furan-dicarboxylic acid (FDA), and 3,5-pyrazole-dicarboxylic acid. The angles formed by the two meta-positional carboxylates in these five-member-ring linkers fall between those of BDC (180°) and IPA (120°), allowing better compatibility in terms of coordination and connection with diverse metal ions.[39–41] As a result, they have the potential to function similarly to IPA molecules for isostructural expansion. However, highly crystalline products obtained by the TDA and FDA linkers separately under slightly modified reaction conditions displayed different PXRD patterns than those of the UTSC-701 series. This indicates the formation of a new phase, which was designated USTC-702 (Figure 3a). Owing to the superior crystallinity of the TDA-related product (USTC-702-TDA), structural analysis was carried out on this sample with the assistance of cRED. The corresponding results confirm that an unreported 3D crystal structure was generated by these five-member-heterocycle linkers. (Note S2, Figure S8 and Tables S5 and S6).

USTC-702-TDA crystallizes in the tetragonal $I422$ (97) space group, with unit cell parameters of $a = b =$ 23.1 Å and $c = 8.0$ Å.[38] The structure features a Ti_8-cycle building unit that maintains the same configuration as the USTC-701 series, consisting of eight bridging acetates and eight carboxylates from TDA linkers. Notably, the eight TDA molecules can be categorized into two groups on the basis of their spatial extension directions (Figure 3b). This includes those arranged clockwise (based on the direction of the sulfur atoms), pointing out of the cluster plane (marked in purple), and those arranged anticlockwise, pointing inward to the cluster plane (marked in green). In this scenario, each TDA linker connects one adjacent cluster, creating an 8-connected structural node, which differs significantly from that in the USTC-701 compounds. A 1D channel-like accessible cavity surrounded by Ti_8 clusters was found running along the c-axis of the structure, with an approximate diameter of 6.0 Å (Figure 3c). Unlike the 2D-layered arrangement of Ti_8 cycles in the structure of USTC-701, neighboring Ti_8 building units in USTC-702 adopt a staggered pattern to reduce steric hindrance (Figure 3d, Figure S9).

To elucidate the potential mechanism underlying the experimental observation that six-member-ring linkers yield 2D structures while five-member-heterocycle linkers lead to 3D structures under similar reaction conditions, density functional theory (DFT) calculations were performed (Note S3). The aim was to investigate the hypothetical formation of 2D versus 3D structures with TDA and 5-CH_3-IPA, respectively. This was achieved by constructing these structures through a ligand replacement strategy applied to existing frameworks, followed by full DFT-geometry optimization. The resulting hypothetical structures, along with their unit cell parameters, are summarized in Figure S10 and Table S7. Additionally, Table S8 provides an overview of their total electronic energy. Notably, these calculations predict that the most stable structures formed with 5-CH_3-IPA and TDA are indeed 2D and 3D in nature, respectively, which aligns with the experimental findings. However, it is important to highlight that the relative energies associated with forming 2D versus 3D configurations ($\Delta E_{2D\rightarrow3D}$) differ significantly depending on the linker used: for example, while $\Delta E_{2D\rightarrow3D}$ values are relatively small (0.16 meV atom^{-1}) for the 5-CH_3-IPA ligand, suggesting that both types of structure could be formed; in contrast, for TDA, the predicted stability of its respective 3D phase far surpasses that of its corresponding 2D counterparts (by a margin of approximately 3.79 meV atom^{-1}). This implies a clear preference toward favoring the formation of a 3D phase when TDA is utilized as a linker material.

To gain deeper insight into the underlying origins of the electronic energy trend observed in 2D versus 3D structures, a comprehensive analysis was conducted on the geometric characteristics of the 5-CH_3-IPA and TDA ligands within their respective DFT-optimized 2D and 3D structures.

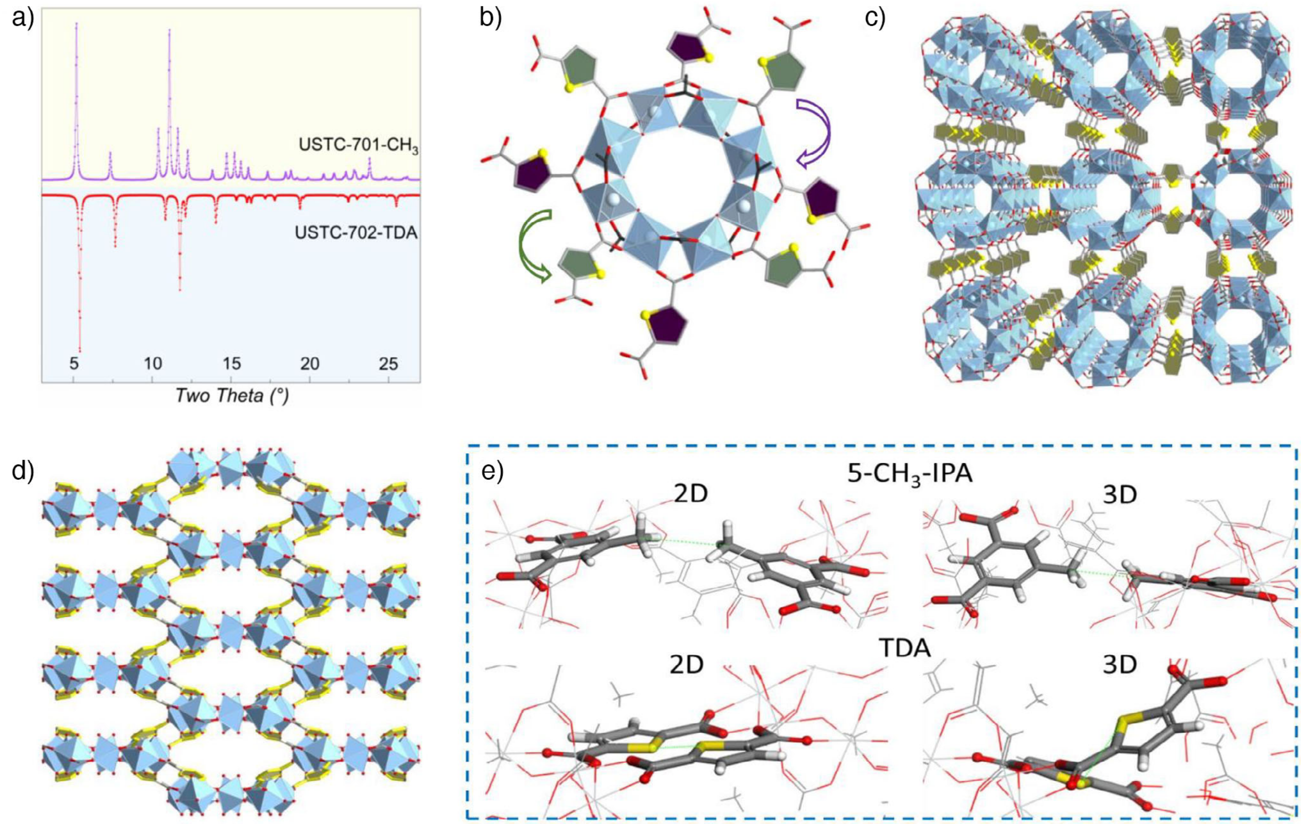

Figure 3. Structural information of USTC-702. a) Comparison of the PXRD patterns of USTC-701-CH$_3$ and USTC-702-TDA. b) Ti$_8$-cycle building unit in the structure of USTC-702-TDA. Eight TDA linker molecules are classified into two groups: those oriented clockwise according to the direction of the sulfur atoms in the thiophene rings pointing out of the Ti$_8$-cycle plane (purple five-membered rings) and those oriented anticlockwise, pointing away from the Ti$_8$-cycle plane (green five-membered rings). c) Central-projection view of the 3D structure of USTC-702-TDA along the *c*-axis, showing accessible voids (thiophene rings are marked in yellow). d) 3D structure of USTC-702-TDA viewed along the *b*-axis, showing that TDA linkers connect Ti$_8$ clusters located in different planes (acetates in Ti$_8$ clusters are omitted for clarity). e) Perspective view of the closest 5-CH$_3$-IPA (top) and TDA (bottom) ligand neighbors within their respective 2D (left) and 3D (right) phases. The dashed green lines represent the distances taken as references to measure the interaction between the ligand dimers (details in Table S9). Color code: Titanium, blue; carbon in the linker carboxylate group, light gray; carbon in the terminal ligand, dark gray; oxygen in the linker carboxylate group, red; oxygen in the terminal ligand and bridging hydroxyl group, light red; oxygen in the bridging oxo group, pink.

Notably, the structures derived from 5-CH$_3$-IPA exhibit significant steric hindrance as a result of the close proximity between neighboring ligands. Specifically, examination of the distances between opposing 5-CH$_3$-IPA ligands (Figure 3e top) revealed measurements of 3.92 aand 3.12 Å in the context of their respective 2D and 3D configurations, thereby indicating that van der Waals interactions may contribute to partial destabilization of the latter phase owing to shorter intermolecular contacts involving opposite linkers. In contrast, TDA did not have significant steric effects on either the 2D or 3D structures because of its smaller size. However, the neighboring TDA thiophene rings in the 2D phase are positioned much closer together than those in the 3D phase are. This is supported by the lower inter-ligand S–S thiophene ring distances of 3.89 and 5.19 Å for the 2D and 3D phases, respectively (Figure 3e bottom).

To further assess the impact of these distinct inter-ligand contacts on the stability of the 2D and 3D structures, we calculated the interaction energies between the two closest neighboring ligands. This was accomplished by comparing the energy difference between the fixed geometries adopted by the ligands in their respective structures and two isolated 5-CH$_3$-IPA/TDA molecules (Table S10). Notably, the interaction energy calculated for the geometry of the 5-CH$_3$-IPA ligands in the 3D structure is positive, indicating that this conformation is highly energetically unfavorable. In contrast, in the case of the 2D structure, the corresponding interaction energy is negative, contributing to stabilizing its architecture. For TDA-related structures, 2D phase neighbors exhibited large positive interaction energies (0.22 eV) compared with those displayed by 3D phases (0.09 eV). Additionally, DFT-optimized analysis revealed that thiophene rings in the 2D structure were more distorted than their counterparts in 3D analogs (Figure S11b). To quantify this distortion, we computed distances between the plane containing carboxylic anchoring groups and the center of the thiophene ring (Figure S11a). Consistent with our previous observation, these distances were negligible for 3D structures (0.01 Å), whereas they amounted to 0.12 Å for those in the 2D phase. As a result, the energies of the isolated TDA ligands in their respective configurations were approximately 0.77 meV atom^{-1} lower than those from a hypothetical phase. Therefore, the close contacts between the TDA thiophene rings resulted in high destabilization and low ligand planarity within their 2D phase, which hindered the formation of this hypothetical phase.

Notably, gradual expansion of the structural cavity along with an increase in thermal stability can be observed when the structures of USTC-701, USTC-702, and MIL-125 are compared (Figures S12–S14). This expansion occurs as the angle between two coordinative carboxylates in IPA increases from 120° to 150° in TDA[42] and finally to 180° in BDC. The intrinsic molecular steric hindrance alteration of the corresponding linkers leads to a change in the connection number of the Ti_8-cycle node, increasing from 4 in USTC-701 to 8 in USTC-702 and ultimately reaching 12 in MIL-125. Our results suggest that other isostructural series of Ti_8-cycle-based frameworks could be synthesized by adjusting the reaction conditions. For example, the assembly of an 8-connected Ti_8-cycle with BDC-type linkers may be possible through the introduction of appropriate substitutions aimed at mitigating the spatial steric hindrance posed by the BDC molecule.

The impact of functional groups oriented toward the cavity of a material structure on its properties, such as size, shape, and interactions with guest molecules, can be assessed by observing its response to external stimuli.[5,43] Thus, the sorption of both gas and vapor on the USTC-701 series was conducted to compare the regulatory effect of each substitution on the material cavity.

Nitrogen (N_2) sorption data at 77 K were initially gathered to obtain basic information about the porosity of each compound. Notable differences in N_2 uptake are evident when comparing the sorption isotherms for each isostructure (Figure 4a). These differences correspond to variations in the calculated standard surface areas and free pore volumes, which are defined as the surface area and cavity volume of one gram of sorbent with units of $m^2\ g^{-1}$ and $cm^3\ g^{-1}$, respectively (Table S11). For example, the isotherm of USTC-701-Br (green spheres) shows a decrease in uptake of approximately 18% in the relative pressure range of 0.1–0.9 compared with that of the nonfunctionalized USTC-701-H (black spheres), resulting in a notably lower Brunauer–Emmett–Teller (BET) area and pore volume than those of USTC-701-H, with an approximately 17% discrepancy (S_{BET}: 540 $m^2\ g^{-1}$ vs. 650 $m^2\ g^{-1}$; V_{pore}: 0.19 $cm^3\ g^{-1}$ vs. 0.23 $cm^3\ g^{-1}$).

However, the introduction of substituted groups results in changes in both the molecular mass of the matrix and the pore structure, significantly impacting the calculations of the standard surface area and pore volume from sorption data. To eliminate the influence of changes in molecular mass and directly compare steric hindrance introduced by substitutions on gas sorption performance, N_2 adsorption gravimetric uptakes with a unit of $cm^3\ g^{-1}$ were converted to molar ratios with a unit of mmol mmol^{-1} to assess the N_2 adsorption capacity of one millimolar sorbent (Figure 4b). Although the isotherms of the USTC-701-F (red spheres) and USTC-701-OCH_3 (dark yellow spheres) compounds exhibit steps at different relative pressures, indicating the presence of pores with different diameters possibly induced by structural defects, the isotherms of the other isostructures overlap well regardless of the substitution nature. Correspondingly, the free pore volumes calculated from the molar ratio uptakes are all approximately 0.4 cm^3 mmol^{-1} (Table S11). This observation suggests that modifying the cavity with an irregular shape in the USTC-701 structure through a functional group has a nearly negligible effect on its adsorptive performance when it interacts with small molecules without strong host–guest interactions, such as N_2, in this case.

We subsequently switched the probe molecule from N_2 to carbon dioxide (CO_2), which is recognized for its diverse interactions with host cavities on the basis of the structural active sites of the sorbent material and sorption temperatures.[44] Single-component CO_2 sorption isotherms of the USTC-701 series were obtained at three distinct temperatures (273, 283, and 298 K; Figure 4c,d and Figure S15), enabling a comprehensive assessment of the corresponding adsorption affinities. A comparison of the gravimetric CO_2 uptakes presented in mmol g^{-1} at 298 K reveals clear discrepancies between each isotherm (Figure 4c), akin to those observed with N_2 at 77 K (Figure 4a). Notably, unlike the molar ratio uptake comparison of the N_2 isotherms at 77 K (Figure 4b), the CO_2 adsorption isotherms that exclude mass change effects still significantly differ from each other (Figure 4d). This finding indicates that functional substitution indeed plays a decisive role in affecting the accommodation of CO_2 guest molecules in the material cavity. Although all calculated isosteric heats of adsorption (Q_{st}) within the pressure range of 0–1 bar for the USTC-701 series fall within normal ranges without noticeable distinctions[44] (Figures S16–S18, Table S12), it becomes evident that variable rotation and stretching local flexibility resulting from each substitution leads to differences in CO_2 adsorptive capacity. For example, USTC-701-Br results in the highest CO_2 uptake of 5.4 mmol mmol^{-1} at 298 K, whereas USTC-701-CF_3 results in a decrease of as much as 30%, with the lowest uptake value of only 3.8 mmol mmol^{-1} under similar conditions; however, both have identical Q_{st} values of 34 kJ mol^{-1} for CO_2 adsorption.

The notable disparities in CO_2 sorption induced by substitutions prompted further investigation into the potential for CO_2/N_2 adsorptive separation capability among each candidate within the USTC-701 series. N_2 sorption data at 273, 283, and 298 K were collected to facilitate the calculation of the ideal adsorbed solution theory (IAST) selectivity for CO_2/N_2 separation (Figures S19–S21 and Tables S12 and S13). The highest selectivity observed at 273 K was 177 for the USTC-701-Py compound, which features an aromatic pyridyl nitrogen atom facing the cavity center, which generates a strong interaction with the CO_2 guest. However, as the sorption temperature increased, the increased diffusion of CO_2 inside the cavity significantly weakened the interaction of the pyridine-CO_2 pair, resulting in a sharp decrease in the separation selectivity to 66 at 298 K, corresponding to a decrease of 63%. In contrast, other functional groups showing weak to medium-level interactions with CO_2 lead to much smaller alterations in separation selectivity upon changes in the sorption temperature. For example, USTC-701-H, which

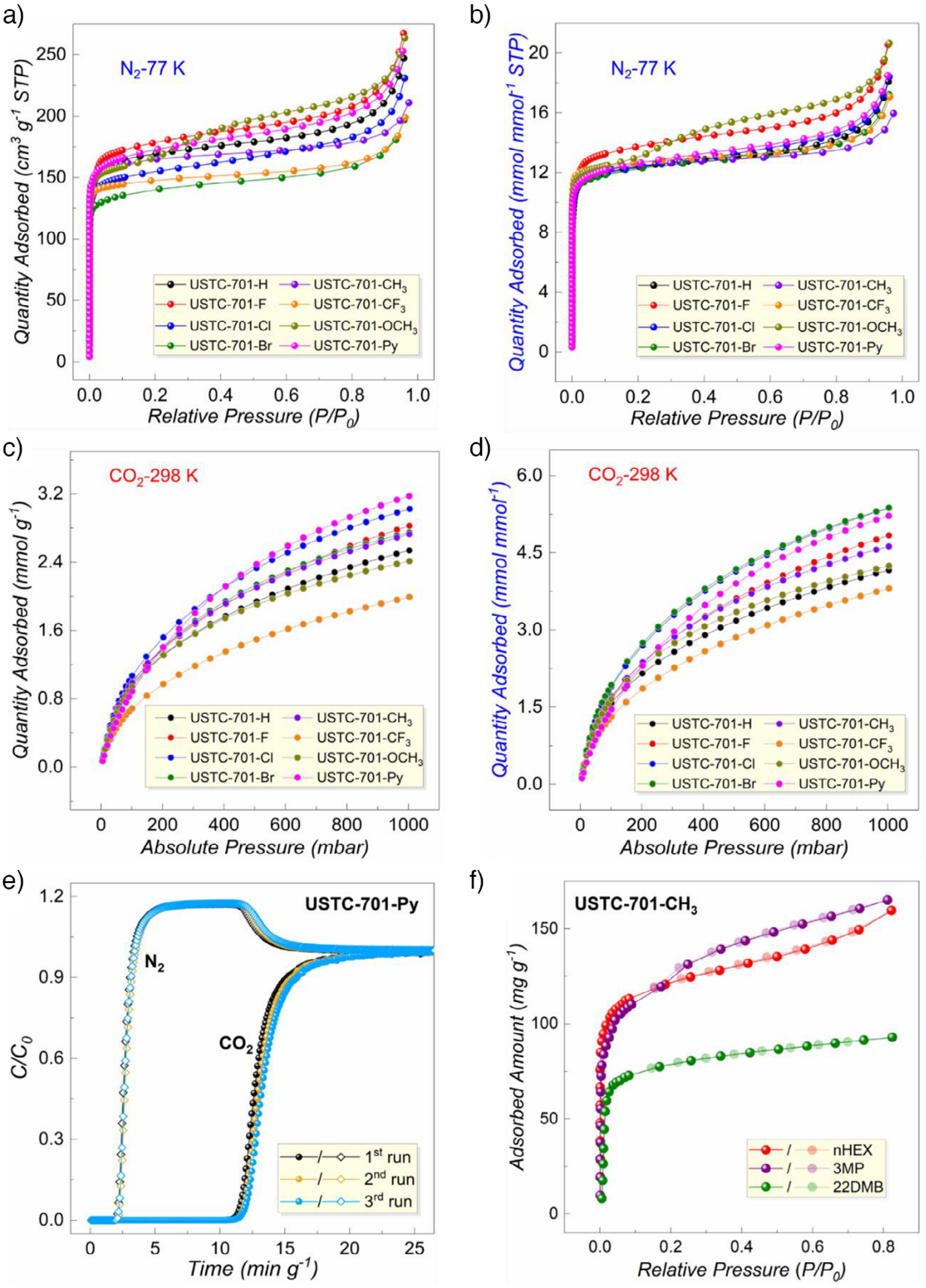

Figure 4. Pore engineering effect in the USTC-701 series as reflected by the response to external stimuli. a) Nitrogen adsorption isotherms of the USTC-701 series collected at 77 K showing gravimetric uptake. b) Nitrogen adsorption isotherms of the USTC-701 series collected at 77 K showing molar ratio uptake. c) Carbon dioxide adsorption isotherms of the USTC-701 series collected at 298 K showing gravimetric uptakes. d) Carbon dioxide adsorption isotherms of the USTC-701 series collected at 298 K showing molar ratio uptakes. e) Column breakthrough curves of USTC-701-Py at 298 K for mixed CO_2/N_2 (15/85 vol%). f) Single-component sorption isotherms of hexane isomers on USTC-701-CH_3 collected at 303 K.

has the highest structural similarity with USTC-701-Py, only displays a 31% decrease in separation selectivity from 90 at 273 K to 62 at 298 K. This highlights the ability of the USTC-701 structure to introduce target functional sites for regulating cavity characteristics and tuning application performance accordingly. Notably, an adjustable range of separation selectivity from 40–72 at 298 K was achieved by introducing different functional groups, demonstrating the substitution-directed pore regulation effect on the material structure.

To further substantiate the efficacy of the USTC-701 series in CO_2/N_2 separation, USTC-701-Py was selected as the representative solid for column breakthrough measurements. The experiments were conducted using a column packed with approximately 1 g of the activated sample at 298 K and 1 bar, employing a mixed gas composition of CO_2/N_2 (15/85 vol%), which simulates typical post-combustion conditions encountered in vacuum swing adsorption processes. As illustrated in Figure 4e, USTC-701-Py has good performance in separating CO_2 from N_2. Notably, N_2 eluted from the column within just 2 min g^{-1}, whereas CO_2 remained adsorbed for an extended duration of up to 11 min g^{-1}. This significantly prolonged retention time for CO_2 compared with N_2 underscores its preferential adsorption by the sorbent, aligning seamlessly with findings from single-component adsorption studies. Furthermore, robust cycling performance was observed during the column breakthrough assessments involving USTC-701-Py.

Compared with those of the USTC-701 series, the 3D structures of USTC-702-TDA and USTC-702-FDA, characterized by expanded porosities, exhibit distinct performances in terms of N_2 and CO_2 sorption. Notably, both series maintain an identical ratio of each structural component, thereby sharing the same molecular formula. Generally, USTC-702 has significantly greater gravimetric N_2 uptake than USTC-701-H does, regardless of whether the uptake is expressed in cm^3 g^{-1} or mmol $mmol^{-1}$; this increase is correlated with the increased porosity within the 3D structure of USTC-702 (Figure S22). Similar to the USTC-701 series, both candidates from the USTC-702 group display comparable adsorption isotherms in molar ratio form, indicating similar pore sizes. The primary distinction between these two structures lies in their CO_2 sorption capabilities; this difference may be attributed to a stronger interaction between guest molecules and furan oxygen atoms than to interactions involving thiophene sulfur atoms.[45] Specifically, USTC-702-FDA not only has markedly greater CO_2 uptake than its TDA counterpart but also shows analogous changes in separation selectivity with varying sorption temperatures—similar to those observed for USTC-701-Py (Figures S23–S26, Tables S12–13). Consequently, the gas sorption performances of these two isostructural compounds further underscore the significant pore-regulating effects achieved through functionalized linkers.

As CO_2 serves as a small gas-phase probe, the pore-regulating effect manifests primarily through host–guest interactions. Consequently, we redirected our focus to evaluating the molecular recognition properties of the USTC-701 series concerning larger guest molecules to assess the impact of steric hindrance associated with each substitution. We selected hexane isomers (C6), including linear n-hexane (*n*Hex), monobranched 3-methylpentane (3MP), and dibranched 2,2-dimethylbutane (22DMB), as representative systems. These aliphatic molecules not only exhibit significant differences in shape and size but also possess inherent structural flexibility. Single-component sorption isotherms of hexane isomers indicate that the cavity in each USTC-701 structure is accessible to all three C6 isomers, demonstrating a logical variation in uptake corresponding to the size and shape differences among these isomers. This results in suboptimal separation performance (Figure S27). Notably, certain substitutions with appropriate sizes and shapes, such as -CH_3, exhibit a pore-opening effect toward 3MP, which has a medium molecular diameter relative to those of the other isomers (Figure S27). As illustrated in Figure 4f, the 3MP uptake by USTC-701-CH_3 remains lower than that of *n*Hex at relative pressures below 0.2. However, a sudden increase in 3MP uptake surpassing that of *n*Hex occurs at 0.3 P/P_0, which is correlated with the pore-opening effect that significantly enhances the adsorption capacity. In the pressure range above 0.3 P/P_0, the uptake of 3MP consistently exceeds that of *n*Hex—an observation rarely noted in C6 adsorptive separation applications.[46] This pore-opening phenomenon may arise from the synergistic effects of an appropriately sized -CH_3 group combined with the rotational and stretching flexibility of the C—C bond. To further validate this hypothesis, benzene and cyclohexane sorption experiments were conducted on USTC-701-CH_3. Both guest molecules indeed produced steps in their adsorption isotherms corresponding to pore openings at varying relative pressures (Figure S28). We propose that pore opening represents a general phenomenon for USTC-701 structures when interacting with specific guest molecules—provided that a functional group with a suitable size and shape alongside an optimized sorption temperature exists. These findings demonstrate not only the local flexibility within the pore environment of USTC-701 but also its potential as an ideal platform for introducing specific functional groups tailored for targeted applications.

Titanium compounds are widely acknowledged for their distinctive photoresponsive properties.[47] Notably, significant advancements have been made over the past decade in various optoelectronic applications of titanium coordination polymers.[17] Considerable focus within this research domain has been directed toward the NH_2-MIL-125 compound and its derivatives. The ortho-position of 2-NH_2-BDC and its diverse derivatives can substantially influence the optoelectronic performance of MOF structures.[23] thereby underscoring the potential and feasibility of pore regulation of their corresponding optoelectronic characteristics. In this context, investigating the effects of pore regulation in the USTC-701 series resulting from various substitutions on their respective optoelectronic performances is imperative.

Ultraviolet–visible (UV–vis) absorption spectra data were initially acquired from the solid samples to elucidate the fundamental optical characteristics of the USTC-701 and USTC-702 compounds. The UV spectra of all members of the USTC-701 series consistently revealed a shoulder absorption peak within the wavelength range of 280–320 nm, which may be attributed to synergistic effects stemming from various substitutions on the benzene rings and their coordination linkages (Figure 5a). USTC-701-OCH_3 exhibited a pronounced redshift in the absorbance wavelength, extending to 370 nm, which corresponds to an optical band gap of 3.36 eV. However, the underlying reasons for this phenomenon are multifaceted and complex. On the one hand, the strong electron-donating influence exerted by the meta-oriented OCH_3 group may play a pivotal role. Conversely, the impact of structural defects—evidenced by nitrogen sorption results—cannot be overlooked.[48] Consequently, it remains challenging to definitively conclude that meta-oriented functional groups with significant electronic effects are instrumental in modulating the electronic structures of isostructurally coordinated compounds at this juncture.

Furthermore, USTC-701-Py—a compound characterized by its well-established electron-deficient pyridyl moiety—displays the highest band gap within this isostructural series at 3.64 eV (341 nm in wavelength). This value closely aligns

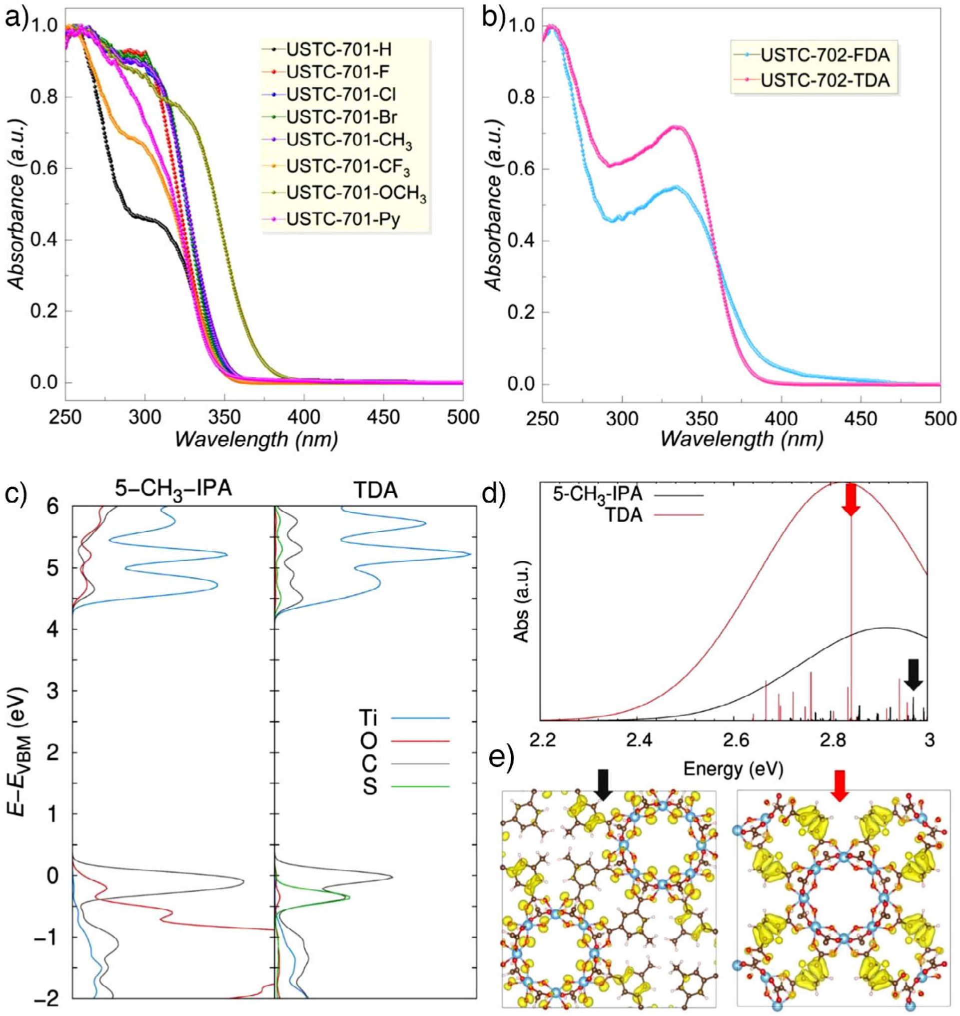

Figure 5. Pore engineering effects on the tuning of optoelectronic responses in the USTC-701 series. a) UV–vis absorption spectra of the USTC-701 series. b) UV–vis absorption spectra of the USTC-702 series. c) Projected density of states (PDOS) for the atoms constituting the USTC-701-CH_3 and USTC-702-TDA frameworks, where the valence band maximum (VBM) energy is set as an energy reference. d) Lowest energy region simulated absorption spectra of USTC-701-CH_3 and USTC-702-TDA compounds, as obtained by convolution of Gaussian functions of the excited state oscillator strengths (vertical lines) with a half-width at full length of $\sigma = 0.15$ eV. e) Top view of unit cells representing the hole distribution corresponding to the main occupied crystalline orbital involved in the transitions marked with black (USTC-701-CH_3) and red (USTC-702-TDA) arrows in the simulated spectra. The excited state characteristics of these vertical transitions are reported in Table S15. The isovalue used to plot the isodensity shapes was set to 0.02 a.u.

with those observed among other members of this series (ranging from 3.58 to 3.62 eV; see Table S14). Notably, these observations regarding the band gap distribution among USTC-701 compounds underscore that substitutions exhibiting weak electronic effects at the fifth position of IPA—particularly ortho–para-oriented functional groups—exert minimal influence on altering the electronic structure of these coordination complexes. In stark contrast to the USTC-701 series, the USTC-702 compounds exhibit UV–vis spectra characterized by distinctly different shapes and absorbance wavelengths (Figure 5b). Notably, two prominent absorption peaks are discerned at 255 and 335 nm for both the TDA and FDA derivatives. The particularly striking peak at 335 nm underscores a significant divergence in the electronic structures between the 2D USTC-701 and 3D USTC-702 frameworks. The band gaps of USTC-702-TDA and USTC-702-FDA were calculated to be 3.30 and 3.22 eV, respectively, on the basis of their absorption in the lowest energy region—values that are markedly lower than those observed within the USTC-701 series.

To elucidate the distinctions in optical responses between these two isostructural families, we conducted DFT calculations on USTC-701-CH_3 and USTC-702-TDA, which serve as representative candidates for each family. In the initial phase of our investigation, we meticulously computed the electronic structures of both materials to assess how ligand variations influence their band edge characteristics. To facilitate this analysis, we illustrated the projected density of states (PDOS) corresponding to the atomic constituents within their frameworks (Figure 5c). Consistent with findings reported for other Ti-based MOFs,[23,49] the conduction band (CB) predominantly localizes around the metal nodes, whereas the valence band (VB) edge is primarily constituted by ligand states. This configuration engenders a ligand-to-metal charge transfer (LMCT) character for transitions occurring at lower energy levels between bands. Consequently, although both 2D and 3D structures exhibit analogous compositions at their CB edges—centered around Ti d states—the nature of their VB edges diverges significantly. In particular, for the 2D structure, a notable degree of delocalization is evident among the oxygen states associated with the Ti_8 cluster; conversely, in the case of the 3D structure, the VB states are entirely delocalized along the thiophene ring states—a phenomenon attributable to increased π-conjugation and pronounced electron-donating properties of such ligands. Owing to these differences in electronic architecture, we found that the computed electronic gap (E_g) for 3D USTC-702-TDA is approximately 0.15 eV lower than its 2D counterpart—an observation that aligns qualitatively with trends discerned from UV–vis spectral analyses.

Nonetheless, the gap values presented herein are derived from absorption band edge measurements, thereby providing the optical gap of the material—an aspect that cannot be discerned from a ground state perspective. To bridge this knowledge gap, we conducted TD-DFPT calculations to investigate the absorption characteristics of both 2D and 3D structures within their lowest energy absorption region. Notably, the simulated absorption spectra depicted in Figure 5d demonstrate that while the 3D structure exhibits pronounced band edge absorption with a distinct peak in this energy range—also corroborated by the UV–vis spectra shown in Figure 5b—the 2D structures display a more subdued absorption profile characterized by states associated with weak transition dipole moments (approximately one order of magnitude lower than those of their 3D counterparts). To elucidate this contrasting absorption behavior, we plotted the crystalline orbitals (COs) contributing to the most significant states within the lowest energy absorption region (Figure 5e and Figure S29). Indeed, the weak absorption observed for the 2D lowest energy states can be attributed to hole delocalization around highly localized O 2p states, which stands in stark contrast to the fully delocalized holes along the thiophene bridges present in the 3D structures. Given their sharp lowest energy absorptions, it is anticipated that the optical gaps obtained from band edge measurements for 3D structures will be significantly lower than those derived from their corresponding 2D structures. This partially explains the deviation between the DFT-computed 3D versus 2D electronic gap (0.15 eV) and the gap difference measured from the UV–vis spectra (0.28 eV).

Finally, with the objective to identify the origin of the bandgap difference between USTC-701 and USTC-702 (nature of the linkers vs. dimensionality), we computed the bandgaps for the fully optimized cells of both 2D (USTC-701) and 3D (USTC-702) MOFs within $-CH_3$ and -TDA linkers. The corresponding data are reported in Table S17. Interestingly, the difference in the calculated band gaps between the 3D vs. 2D structures with the same linker is minimal (0.03–0.07 eV), while, on the other hand, TDA linker-based structures exhibit bandgaps systematically lower (0.31–0.39 eV) with respect to the ones shown by the $-CH_3$ linkers-based derivatives, independently of the dimensionality or the DFT functional considered (see Table S17). Therefore, we can conclude that linker engineering remains the most effective strategy to tune the bandgaps of this family of materials.

Moreover, the hydrogen evolution reaction driven by visible light was selected as the model system to evaluate the influence of pore regulation on the photocatalytic efficacy of the USTC-701 derivatives. Notably, a direct comparison of the photocatalytic performance of various reported catalysts for hydrogen evolution has limited scientific value, given that documented reaction systems, conditions, and evaluation methodologies encompass a vast array of flexible parameters. Consequently, the assessment of the photocatalytic activity of USTC-701 isostructures derived under uniform conditions is aimed primarily at elucidating the structure–performance relationship. In light of this consideration, four representative candidates were meticulously curated on the basis of several pivotal criteria: 1) USTC-701-H serves as a nonfunctionalized reference compound; 2) USTC-701-F demonstrates minimal substitution effects and is extensively characterized for its hydrophobic attributes; 3) USTC-701-Br offers an alternative preferred orientation during crystal growth, with the -Br group introducing considerable steric hindrance; and 4) USTC-701-Py is distinguished by its hydrophilic pyridyl moiety while exhibiting comparable steric hindrance akin to that of USTC-701-H.

These four isostructural compounds were employed as photocatalysts in the hydrogen evolution reaction (Note S1). Although the reference compound USTC-701-H exhibited a H_2 production rate of 406 ± 17 µmol g^{-1} h^{-1}, the hydrophobic variant USTC-701-F demonstrated a significant decrease in catalytic performance, yielding a H_2 production rate of only 138 ± 2 µmol g^{-1} h^{-1} (Figure S31). This dramatic reduction—approximately 66% relative to the reference value—can likely be attributed to the restricted accessibility of catalytically active sites for water molecules due to the hydrophobic nature of the -F groups oriented toward the pore openings.[50] In stark contrast, hydrophilic USTC-701-Py has a notable increase in catalytic activity, achieving a H_2 production rate of 812 ± 33 µmol g^{-1} h^{-1}—twice that of its reference counterpart—underscoring the advantageous role played by accessible hydrophilic substitutions in increasing photocatalytic efficacy. Furthermore, USTC-701-Br resulted in a H_2 production rate of 441 ± 4 µmol g^{-1} h^{-1}, which was comparable to that observed with the reference compound. This observation leads us to several potential conclusions: 1) The preferred orientation for crystal growth has a minimal influence on the catalytic performance; 2) the pronounced steric hindrance associated with -Br substitution does not adversely affect the catalytic activity, possibly owing to the decrease in the molecular size of water; and 3) the -Br group has a significantly weaker hydrophobicity than the -F group does, thereby exerting a limited impact on the overall catalytic efficiency. Consequently, our findings suggest that despite their analogous electronic structures among isostructural members, the modulation of hydrophilicity/hydrophobicity through functional groups plays a pivotal role in fine-tuning the photocatalytic activity during water-splitting reactions.

This insight could prove invaluable for future endeavors aimed at designing advanced photocatalysts tailored for water-splitting applications.

Conclusions

In comparison to other functionalized benchmark compounds and previously reported isostructural coordination polymers, USTC-701 and USTC-702 provide a unique platform for evaluating the individual effects of specific substitutional groups on their properties. This capability arises from the distinctive characteristics of isophthalate-type linkers, which can effectively differentiate each influential parameter of functional groups located away from the benzene ring's coordinative sites. The introduction of functional groups into the pore environment—regardless of size, mass, or electronic properties—has minimal impact on how the pore structure responds to small non-interactive probe molecules like N_2 when there are no access constraints. In contrast, steric hindrance and vibrational capabilities associated with these functional groups significantly affect molecular recognition processes when probe molecules are appropriately sized and interactive; this is particularly evident with CO_2 and C6 hydrocarbons. Thus, it becomes feasible to systematically evaluate and categorize the effects arising from the spatial characteristics of functional groups. Additionally, the influence of electronic characteristics related to these groups can be examined separately based on their substitution nature and corresponding photoresponses. Therefore, our findings demonstrate a comprehensive evaluation of the substitution effect and its subsequent impact on pore regulation, as well as the corresponding physical and chemical properties within a meticulously designed material platform. This research holds significant potential in providing valuable guidance for the future design and synthesis of optimal functionalized coordination polymers aimed at important applications.

Methods

Synthesis of USTC-701 and USTC-702

The general synthesis method was as follows: In a 25 mL autoclave reactor, the linker, acetic anhydride (AAD), acetic acid (AA), and MeOH were introduced and stirred at room temperature (RT). While stirring, Ti_8AF was added to the mixture. The reaction mixture was subsequently heated in an oven at either 180 or 200 °C for 72 h. After cooling to RT, the product was collected via centrifugation, washed with acetone, and then air-dried. The detailed reaction conditions for synthesizing each polymer are provided in Table S18.

Sorption of CO_2 and N_2

Single-component adsorption isotherms of CO_2 and N_2 at 273, 283, and 298 K were collected on a Micromeritics 3Flex analyzer. The sample was activated under dynamic vacuum at 423 K for 8 h prior to data collection. The CO_2/N_2 breakthrough test was performed on a BSD-MAB dynamic gas adsorption apparatus. A total of 0.25 g of the USTC-701-Py sample was packed into a glass sample tube (4.0 mm I.D. × 60 mm). The column was first purged with helium at a rate of 14 mL min^{-1} at 423 K for 4 h. The fixed bed was then cooled to the analysis temperature (298 K), and the helium flow was switched to a CO_2/N_2 gas mixture (CO_2: 1.5 mL min^{-1}, N_2: 8.5 mL min^{-1}, total flow rate: 10 mL min^{-1}). The gas concentrations of N_2 and CO_2 at the outlet were measured with an online mass spectrometer.

Photocatalytic Hydrogen Evolution Reaction

The photocatalytic hydrogen production experiments were conducted in a 160 mL optical reaction vessel (Beijing Perfectlight Technology Co., Ltd., China) with stirring at room temperature. The amount of photocatalyst used was 10 mg. The mixture consisted of 18 mL of acetonitrile, 0.2 mL of deionized water, and 2 mL of triethylamine (TEA). The Pt precursor solution (3 wt% of the MOF) was added as a cocatalyst, and after thorough mixing, the suspension was stirred and purged with nitrogen for approximately 20 min to eliminate air. A 300 W Xe lamp served as the illuminant source. For each assessment of hydrogen generation, gas chromatography analysis using argon as the carrier gas and equipped with a Shimadzu GC2014 thermal conductivity detector (TCD), was used to quantify the injected headspace volume of 200 µL by referencing it to an internal hydrogen standard through calibration plotting.

Author Contributions

Conceptualization, S.W., P.G., H.W. and G.M.; Investigation, Q.Y., C.N., V.C., F.G., Y.D., H.X., H.W., G.M., P.G., and S.W.; Writing—Original Draft, S.W., V.C; Writing—Review & Editing, Q.Y., C.N., V.C., F.G., Y.D., H.X., H.W., G.M., P.G., and S.W.; Supervision, S.W., P.G., H.W., and G.M.

Acknowledgements

Q.Y., Y.D., and S.W. express their gratitude for the financial support received from the National Natural Science Foundation of China (Grant No. 22071234), the Fundamental Research Funds for the Central Universities (WK9990000113 and WK2480000007), and the CAS Talent Introduction Program (Category B, Grant KJ9990007009). They also acknowledge Dr. Kang Sun and Prof. Hailong Jiang from the University of Science and Technology of China for their invaluable assistance in photocatalysis. G.M. extends his appreciation to Institut Universitaire de France for awarding him a Senior Chair position. V.D.-C. and G.M. are grateful to METHASOL H2020-LC-SC3-RES-3–2020 (GA No. 101022649) and MOF2H2 (GA No. 101084131) projects for their financial backing, as well as to GENCI-CINES (Grant A0160907613) and Très Grand Centre de Calcul (TGCC)-CEA facilities for providing high-performance computing resources. F.G., H.X., and H.W. acknowledge funding support from the National Natural Science Foundation of China (No. 22478251) and the Shenzhen Science and Technology Program (No. KCXFZ20211020163818026). The material characterization conducted in this study was partially facilitated by the Instruments Center for Physical Science at the University of Science and Technology of China. The authors would like to convey their sincere thanks to Dr. Yinhua Zhao, Dr. Wanting Liu, Dr. Mei Sun, and Dr.Jun Zhou for their valuable contributions and insightful discussions throughout this work.

Conflict of Interests

The authors declare no conflict of interest.

Data Availability Statement

All data involved in this work are included in this article and the corresponding supplementary materials. The crystal structures of USTC-701-CH^3, USTC-701-Br and USTC-702-TDA are available in the CCDC database under CCDC-2381710, 2353468 and 2353466.

Keywords: Guest-responsiveness • Isostructural functionalization • Pore engineering • Titanium-MOFs

[1] P. Guo, J. Shin, A. G. Greenaway, J. G.i Min, J. Su, H. J. Choi, L. Liu, P. A. Cox, S. B. Hong, P. A. Wright, X. Zou, *Nature* **2015**, *524*, 74–78.
[2] Z. R. Gao, H. Yu, F.-J. Chen, A. Mayoral, Z. Niu, Z. Niu, X. Li, H. Deng, C. Márquez-Álvarez, H. He, S. Xu, Y. Zhou, J. Xu, H. Xu, W. Fan, S. R. G. Balestra, C. Ma, J. Hao, J. Li, P. Wu, J. Yu, M. A. Camblor, *Nature* **2024**, *628*, 99–103.
[3] S. Kitagawa, R. Matsuda, *Coord. Chem. Rev.* **2007**, *251*, 2490–2509.
[4] C. Gu, N. Hosono, J.-J. Zheng, Y. Sato, S. Kusaka, S. Sakaki, S. Kitagawa, *Science* **2019**, *363*, 387–391.
[5] W. Fan, X. Zhang, Z. Kang, X. Liu, D. Sun, *Coord. Chem. Rev.* **2021**, *443*, 213968.
[6] P. Nugent, Y. Belmabkhout, S. D. Burd, A. J. Cairns, R. Luebke, K. Forrest, T. Pham, S. Ma, B. Space, L. Wojtas, M. Eddaoudi, M. J. Zaworotko, *Nature* **2013**, *495*, 80–84.
[7] H. Jiang, D. Alezi, M. Eddaoudi, *Nat. Rev. Mater.* **2021**, *6*, 466–487.
[8] M. Eddaoudi, J. Kim, N. Rosi, D. Vodak, J. Wachter, M. O'Keeffe, O. M. Yaghi, *Science* **2002**, *295*, 469–472.
[9] Z. Chen, P. Li, R. Anderson, X. Wang, X. Zhang, L. Robison, L. R. Redfern, S. Moribe, T. Islamoglu, D. A. Gómez-Gualdrón, T. Yildirim, J. F. Stoddart, O. K. Farha, *Science* **2020**, *368*, 297–303.
[10] H. Deng, S. Grunder, K. E. Cordova, C. Valente, H. Furukawa, M. Hmadeh, F. Gándara, A. C. Whalley, Z. Liu, S. Asahina, H. Kazumori, M. O'Keeffe, O. Terasaki, J. F. Stoddart, O. M. Yaghi, *Science* **2012**, *336*, 1018–1023.
[11] B. Li, H.-M. Wen, H. Wang, H. Wu, T. Yildirim, W. Zhou, B. Chen, *Energy Environ. Sci.* **2015**, *8*, 2504–2511.
[12] N. Huang, S. Yuan, H. Drake, X. Yang, J. Pang, J. Qin, J. Li, Y. Zhang, Q.i Wang, D. Jiang, H.-C. Zhou, *J. Am. Chem. Soc.* **2017**, *139*, 18590–18597.
[13] T. Devic, P. Horcajada, C. Serre, F. Salles, G. Maurin, B. Moulin, D. Heurtaux, G. Clet, A. Vimont, J.-M. Grenèche, B. L.e Ouay, F. Moreau, E. Magnier, Y. Filinchuk, J. Marrot, J.-C. Lavalley, M. Daturi, G. Férey, *J. Am. Chem. Soc.* **2010**, *132*, 1127–1136.
[14] A. Buragohain, P. Van Der Voort, S. Biswas, *Microporous Mesoporous Mater.* **2015**, *215*, 91–97.
[15] A. H. Assen, K. Adil, K. E. Cordova, Y. Belmabkhout, *Coord. Chem. Rev.* **2022**, *468*, 214644.
[16] R. Banerjee, A. Phan, B. Wang, C. Knobler, H. Furukawa, M. O'Keeffe, O. M. Yaghi, *Science* **2008**, *319*, 939–943.
[17] Y. Du, Q. Yan, S. Wang, *Small* **2024**, *20*, 2403470.
[18] H. Assi, G. Mouchaham, N. Steunou, T. Devic, C. Serre, *Chem. Soc. Rev.* **2017**, *46*, 3431–3452.
[19] H.a L. Nguyen, T. T. Vu, D. Le, T. L. H. Doan, V. Q. Nguyen, N. T. S. Phan, *ACS Catal.* **2017**, *7*, 338–342.
[20] C. Li, H. Xu, J. Gao, W. Du, L. Shangguan, X. Zhang, R.-B. Lin, H. Wu, W. Zhou, X. Liu, J. Yao, B. Chen, *J. Mater. Chem. A* **2019**, *7*, 11928–11933.
[21] J. T. Bryant, M. W. Logan, Z. Chen, M. Djokic, D. R. Cairnie, D. A. Vazquez-Molina, A. Nijamudheen, K. R. Langlois, M. J. Markley, G. Pombar, A. A. Holland, J. D. Caranto, J. K. Harper, A. J. Morris, J. L. Mendoza-Cortes, T. Jurca, K. W. Chapman, F. J. Uribe-Romo, *J. Am. Chem. Soc.* **2023**, *145*, 4589–4600.
[22] M. Dan-Hardi, C. Serre, T. Frot, L. Rozes, G. Maurin, C. Sanchez, G. Férey, *J. Am. Chem. Soc.* **2009**, *131*, 10857–10859.
[23] C. H. Hendon, D. Tiana, M. Fontecave, C. Sanchez, L. D'arras, C. Sassoye, L. Rozes, C. Mellot-Draznieks, A. Walsh, *J. Am. Chem. Soc.* **2013**, *135*, 10942–10945.
[24] M. Ding, R. W. Flaig, H.-L. Jiang, O. M. Yaghi, *Chem. Soc. Rev.* **2019**, *48*, 2783–2828.
[25] Y. Sun, D.-F. Lu, Y. Sun, M.-Y. Gao, N. Zheng, C. Gu, F. Wang, J. Zhang, *ACS Materials Lett.* **2021**, *3*, 64–68.
[26] S. Wang, H. Reinsch, N. Heymans, M. Wahiduzzaman, C. Martineau-Corcos, G. De Weireld, G. Maurin, C. Serre, *Matter* **2020**, *2*, 440–450.
[27] Y. Bai, Y. Dou, L.-H. Xie, W. Rutledge, J.-R. Li, H.-C. Zhou, *Chem. Soc. Rev.* **2016**, *45*, 2327–2367.
[28] R. G. Pearson, *J. Am. Chem. Soc.* **1963**, *85*, 3533–3539.
[29] O. T. Qazvini, R. Babarao, Z.-L. Shi, Y.-B. Zhang, S. G. Telfer, *J. Am. Chem. Soc.* **2019**, *141*, 5014–5020.
[30] S. A. Bourne, J. Lu, A. Mondal, B. Moulton, M. J. Zaworotko, *Angew. Chem. Int. Ed.* **2001**, *40*, 2111–2113.
[31] S. Wang, L. Chen, M. Wahiduzzaman, A. Tissot, L. Zhou, I. A. Ibarra, A. Gutiérrez-Alejandre, J. S. Lee, J.-S. Chang, Z. Liu, J. Marrot, W. Shepard, G. Maurin, Q. Xu, C. Serre, *Matter* **2021**, *4*, 182–194.
[32] Y. Wang, S. Takki, O. Cheung, H. Xu, W. Wan, L. Öhrström, A. K. Inge, *Chem. Commun.* **2017**, *53*, 7018–7021.
[33] C. Nie, N. Yan, C. Liao, C. Ma, X. Liu, J. Wang, G. Li, P. Guo, Z. Liu, *J. Am. Chem. Soc.* **2024**, *146*, 10257–10262.
[34] J. Wang, C. Ma, J. Liu, Y.i Liu, X. Xu, M. Xie, H. Wang, L. Wang, P. Guo, Z. Liu, *J. Am. Chem. Soc.* **2023**, *145*, 6853–6860.
[35] X. Liu, L. Liu, T. Pan, N. Yan, X. Dong, Y. Li, L. Chen, P. Tian, Y.u Han, P. Guo, Z. Liu, *Angew. Chem. Int. Ed.* **2021**, *60*, 24227–24233.
[36] T. Yang, T. Willhammar, H. Xu, X. Zou, Z. Huang, *Nat. Protoc.* **2022**, *17*, 2389–2413.
[37] Y. Liu, X. Liu, A. Su, C. Gong, S. Chen, L. Xia, C. Zhang, X. Tao, Y. Li, Y. Li, T. Sun, M. Bu, W. Shao, J. Zhao, X. Li, Y. Peng, P. Guo, Y. U. Han, Y. Zhu, *Chem. Soc. Rev.* **2024**, *53*, 502–544.
[38] Deposition Numbers 2381710 (for USTC-701-CH$_3$), 2353468 (for USTC-701-Br) and 2353466 (for USTC-702-TDA) contain the supplementary crystallographic data for this paper. These data are provided free of charge by the joint Cambridge Crystallographic Data Centre and Fachinformationszentrum Karlsruhe Access Structures service.

[39] D. Lenzen, J. Zhao, S.-J. Ernst, M. Wahiduzzaman, A. Ken Inge, D. Fröhlich, H. Xu, H.-J. Bart, C. Janiak, S. Henninger, G. Maurin, X. Zou, N. Stock, *Nat. Commun.* **2019**, *10*, 3025.

[40] N. Hanikel, X. Pei, S. Chheda, H. Lyu, W. Jeong, J. Sauer, L. Gagliardi, O. M. Yaghi, *Science* **2021**, *374*, 454–459.

[41] A. Cadiau, J.i S. Lee, D. Damasceno Borges, P. Fabry, T. Devic, M. T. Wharmby, C. Martineau, D. Foucher, F. Taulelle, C.-H.o Jun, Y. K. Hwang, N. Stock, M. F. De Lange, F. Kapteijn, J. Gascon, G. Maurin, J.-S. Chang, C. Serre, *Adv. Mater.* **2015**, *27*, 4775–4780.

[42] T. JM. Ma Ntep, M. Wahiduzzaman, E. Laurenz, I. Cornu, G. Mouchaham, I. Dovgaliuk, S. Nandi, K. Knop, C. Jansen, F. Nouar, P. Florian, G. Füldner, G. Maurin, C. Janiak, C. Serre, *Adv. Mater.* **2024**, *36*, 2211302.

[43] J. F. Kurisingal, D. W. Kim, C. S. Hong, *Coord. Chem. Rev.* **2024**, *507*, 215731.

[44] C. A. Trickett, A. Helal, B. A. Al-Maythalony, Z. H. Yamani, K. E. Cordova, O. M. Yaghi, *Nat. Rev. Mater.* **2017**, *2*, 17045.

[45] J. Hu, Y. Liu, J. Liu, C. Gu, D. Wu, *Microporous Mesoporous Mater.* **2018**, *256*, 25–31.

[46] Z. Zhang, S. B. Peh, C. Kang, K. Chai, D. Zhao, *Energychem* **2021**, *3*, 100057.

[47] X. Chen, A. Selloni, *Chem. Rev.* **2014**, *114*, 9281–9282.

[48] Z. Fang, J. P. Dürholt, M. Kauer, W. Zhang, C. Lochenie, B. Jee, B. Albada, N. Metzler-Nolte, A. Pöppl, B. Weber, M. Muhler, Y. Wang, R. Schmid, R. A. Fischer, *J. Am. Chem. Soc.* **2014**, *136*, 9627–9636.

[49] S. Wang, T. Kitao, N. Guillou, M. Wahiduzzaman, C. Martineau-Corcos, F. Nouar, A. Tissot, L. Binet, N. Ramsahye, S. Devautour-Vinot, S. Kitagawa, S. Seki, Y. Tsutsui, V. Briois, N. Steunou, G. Maurin, T. Uemura, C. Serre, *Nat. Commun.* **2018**, *9*, 1660.

[50] Y. Zhao, K. X. Yao, B. Teng, T. Zhang, Y. Han, *Energy Environ. Sci.* **2013**, *6*, 3684–3692.

Manuscript received: February 13, 2025
Revised manuscript received: April 20, 2025
Accepted manuscript online: April 20, 2025
Version of record online: ■■, ■■

Research Article

Porous Coordination Polymers

Q. Yan, C. Nie, V. D. Cabanes, F.-A. Guo, Y. Du, H. Xia, H. Wang*, G. Maurin*, P. Guo*, S. Wang* ———— **e202503618**

Pore Engineering in Isoreticular Titanium-Isophthalate Coordination Polymers

In this study, we designed titanium-isophthalate coordination polymers with functional groups to regulate pore characteristics and structural dimensionality. We conducted extensive investigations to explore how pore engineering influences adsorptive separation and photoresponsive behavior in these compounds. Our findings address the synthesis challenge of isostructural Ti-coordination polymers and offer insights into structure–property relationships through modulation of their chemical environments.